Journal of Applied Fluid Mechanics, Vol. 19, No. 1, pp. 3170-3188, 2026. Available online at www.jafmonline.net, ISSN 1735-3572, EISSN 1735-3645. https://doi.org/10.47176/jafm.19.1.3722



Numerical Study on Cavitation of Auxiliary Blades Centrifugal Pump under Low Flow Conditions

G. Yi^{1,2,3,4†}, Z. D. Xiao⁵, R. B. Er⁶, L. Hui^{3,4,7}, and Z. X. Ming⁸

¹ Suzhou Vocational University, Suzhou, Jiangsu 215000, China
² Jiangsu Provincial Engineering Research Center for Robotics and Intelligent Equipment, Suzhou, Jiangsu ,215000, China
³ Key Laboratory of Fluid and Power Machinery, Ministry of Education, Xihua University, Cheng Du,
Si Chuan, 610039, China

⁴ Wuxi Kailian technology Co, Ltd, WuXi, Jiangsu, 214142 China
 ⁵ nVent Thermal (Suzhou) Co.,Ltd, Suzhou, Jiangsu, 215031, China
 ⁶ Chery Automobile Co., Ltd, Wuhu, Anhui, 241007, China
 ⁷ School of Energy and Power Engineering, Xihua University, Cheng Du, Si Chuan, 610039, China
 ⁸ Ningbo Autowin Electrical Co., Ltd, Ningbo, Zhejiang, 315042, China

†Corresponding Author Email: 92456@jssvc.edu.cn

ABSTRACT

The auxiliary-blade impeller in a five-stage centrifugal pump was investigated through numerical simulation and experimental validation to ensure the accuracy of finite element analysis results. Based on the Homogeneous Equilibrium Cavitation Model, steady-state calculations were employed to evaluate the cavitation performance of the pump with auxiliary blades. The cavitation mechanism and its variation under different flow rates were studied, with transient cavitation simulations conducted to capture dynamic behaviors. The pressure pulsation coefficient under cavitating conditions was analyzed in the frequency domain using Fourier transform. This study focuses on exploring the cavitation flow mechanism in the auxiliary-blade pump under low-flow conditions and analyzing the evolution mechanism of transient cavitation flow induced by auxiliary blades.It was found that for the multi-stage centrifugal pump with auxiliary blades, a lower flow rate corresponds to a reduced the critical NPSH and enhanced cavitation resistance. When the flow rate decreases to 0.3Q (where Q represents the design flow rate), the critical NPSH decreases by 16% compared to the Q condition. Under varying inlet total pressures, cavitation initially occurs at the suction surface near the blade leading edge. As inlet pressure decreases, the cavitation area gradually expands from the blade suction surface to the entire impeller passage, resulting in a significant drop in pump head. The front chamber of the first-stage impeller maintains relatively high pressure, preventing cavitation during normal operation; after cavitation onset, the flow velocity in the front chamber decreases significantly compared to non-cavitating conditions. Following cavitation in multi-stage centrifugal pumps, internal water pressure exhibits unstable fluctuations. As the number of stages increases, the pressure fluctuation range at the outlet of each stage guide vane increased, and the frequency domain vibration amplitude rises. The water storage chamber at the pump outlet exerts a damping effect, reducing vibration amplitudes. Under this damping effect, the low-frequency vibration amplitude generated by cavitation at the pump outlet is lower than that at the guide vane outlet, with the maximum amplitude decreasing about by 2/3.

Article History

Received June 4, 2025 Revised July 30, 2025 Accepted August 7, 2025 Available online November 5, 2025

Keywords:

Auxiliary blades Centrifugal pump Numerical simulation Unsteady cavitation Amplitude

1. Introduction

Cavitation in multi-stage centrifugal pumps significantly degrades pump performance and may cause

severe cavitation damage to critical components, such as the impeller, during prolonged operation. Therefore, investigating methods to enhance the cavitation resistance of centrifugal pumps is of paramount importance. Chen et al. (2021), selected a high-speed submersible axial flow pump with a specific speed of n_s=700 as their research object to analyze internal cavitation characteristics. They observed that deviations in operating flow rate from design conditions exacerbate cavitation phenomena. In practical engineering applications, increasing the inlet pressure and maintaining the operating flow rate at the design value effectively mitigate cavitation. Zhao et al. (2022), demonstrated that biomimetic structures exert minimal influence on the hydraulic performance of prototype pumps while effectively suppressing cavitation development and reducing cavitation volume. The most pronounced suppression effect occurs during initial cavitation stages, with an average cavitation volume fraction reduction of 99.72%. Biomimetic models thus offer a viable means to suppress cavitation and improve performance in centrifugal pumps. Si et al. (2022), noted significant gaps in understanding the relationship between cavitation vortices and acoustic responses in centrifugal pumps, as well as a lack of comprehensive analysis of these multiscale phenomena in unsteady cavitation flows. They proposed that acoustic boundary condition methods in fluid-structure-sound coupling can accurately predict cavitation noise. Current research frontiers in cavitation suppression include biomimetic design, supercavitation pumps, and noise reduction techniques. Soyama (2021), discovered a strong correlation between vortex cavitation collapse and fluid dynamic cavitation luminescence intensity, proposing an estimation method that incorporates sound velocity. The results aligned closely with measured luminescence intensities. Gohir & Saini (2015), investigated the effects of temperature, inlet total pressure, and flow velocity on flow fields through transient numerical simulations and experimental validation, establishing relationships between cavitation rate and normalized efficiency loss. Yun et al. (2020) indicates that with the development of cavitation, the variation of head with net positive suction head NPSH_a and the variation of head with pressure iso surface area are consistent. Therefore, the area of the pressure iso surface can be used to predict cavitation performance. For specific impeller blades, since the area ratio Rs is proportional to the area of the pressure iso surface, cavitation performance can be predicted through the area ratio R_s , and the

feasibility of this method has been demonstrated through experiments, which will greatly promote the optimization design of pump cavitation performance. Some other scholars have also studied the cavitation phenomenon in fluid machinery. (Li, D. et al., 2022; Li, G. et al., 2022; Lu, et al., 2022; Shi, et al., 2021; Song, et al., 2022; Wei, et al., 2022; Xu, S. et al., 2022; Yan, et al., 2022; Zhao, G. et al., 2021a, b; Zhao, W. et al., 2021

Recent studies indicate that adding auxiliary blades to the impeller front plate alters internal pump flow characteristics and influences cavitation performance. Gao, et al. (2023a, b). However, the impact of auxiliary blades on cavitation characteristics remains underexplored. This study focuses on a five-stage centrifugal pump with auxiliary blades, employing numerical simulation and experimental validation to ensure simulation accuracy. Based on these findings, the cavitation flow mechanism under varying flow rates is investigated, with particular emphasis on internal cavitation characteristics under low-flow conditions.

2. RESEARCH MODEL

2.1 Computational Model

multi-stage centrifugal pump investigation operates under the following specifications: flow rate Q=3.6m³/h, head H=38m, rated speed n=2800rpm, rated power P=1350W, main shaft diameter D_z =14mm, impeller inlet diameter D_i =33.5mm, impeller outer diameter D_2 =103mm, outlet blade width b_2 =3mm, guide vane base circle diameter D₄=104mm, and five impeller stages with auxiliary blades mounted on the outer side of the front cover plate. The geometric model of the pump components and internal water body was constructed using CATIA P3 V5-6R2018 software, followed by assembly. The pump components and water body model are illustrated in Fig. 1. To ensure stable water flow at the inlet and outlet sections and prevent backflow, extension sections were added to both the inlet and outlet domains of the water body (Ji, et al., 2020a,b; Li, W. et al., 2020).

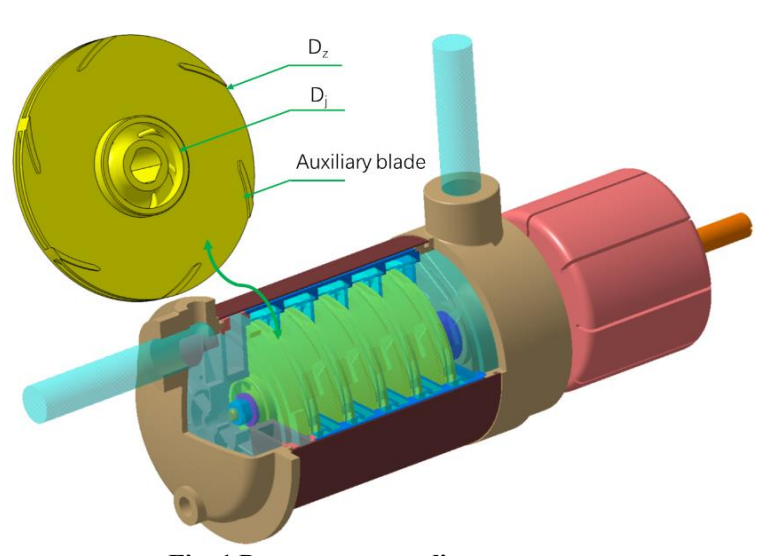


Fig. 1 Pump structure diagram

2.2 Mesh Creation

The water body model was imported into ICEM for mesh generation. To achieve better mesh quality, small faces and sharp corners were locally refined. After mesh generation, mesh quality checks and independence verification were performed (Ji, L., et al., 2023; Qian C., et al., 2021). The final mesh for the computational model in this study consists of 8,021,591 elements, with the main water body mesh shown in Fig. 2. Considering mesh quality, geometric features, and computational resources, the water body was meshed with the following size constraints: in regions without significant turbulence, the maximum mesh size was set to 2.8 to optimize computational efficiency; in areas with small surfaces and sharp corners, the maximum mesh size was limited to 1; and near interface regions, the maximum mesh size was restricted to 0.6.

2.3 Condition Setting and Model Selection

The water body surfaces in contact with solid walls were designated as wall boundaries, while those in contact with other water body regions were defined as interfaces. All fluid domains were modeled as water at 25 °C. The impeller water body was set as a rotating domain with a rotational speed of 2800 rev/min. The calculation equations as shown in formula (1), (2), (3), (4), (5). Numerical simulations were performed using the standard k- ε turbulence model for the fluid domain. The SIMPLEC algorithm was employed to achieve coupled pressure-velocity solutions. Boundary conditions included a

pressure inlet, velocity outlet, adiabatic walls, and standard wall functions (Li, 2012; Liu, et al., 2019; He, X., et al., 2017; Ji, et al., 2020c; Liu, et al., 2022; Fu, et al., 2023; Xu, Z, et al., 2021; Al-Obaidi & Shaban, 2021). The convergence accuracy is 1x10⁻⁴.

$$\frac{\partial \rho}{\partial t} + \nabla(\rho \vec{u}) = 0 \tag{1}$$

$$\frac{\partial(\rho\vec{u})}{\partial t} + (\rho\vec{u}\nabla)\vec{u} = \rho\vec{f} - \nabla p + u\nabla^2\vec{u} + \frac{\mu}{3}\nabla(\nabla\vec{u})$$
 (2)

where t denotes time (s); ∇ denotes the nabla operator; u denotes the velocity vector (m/s); f denotes the mass force vector (m/s²); p denotes the pressure (Pa); The density and dynamic viscosity of the two-phase flow mixture were defined adopting Eqs. (3) – (5).

$$\rho = a_{\nu}\rho_{\nu} + a_{l}\rho_{l} \tag{3}$$

$$\mu = a_v \mu_v + a_l \mu_l \tag{4}$$

$$a_v + a_l = 1 \tag{5}$$

where ρ denotes the density (kg/m³); μ denotes the dynamic viscosity (Pa·s); α denotes the volume fraction. Subscripts ν and l denote the vapor and water liquid, respectively. The state parameters of water vapor were described adopting the transport equation, Eq. (6).

$$\frac{\partial (\rho_{\nu} a_{\nu})}{\partial t} + \nabla (\rho_{\nu} a_{\nu} \vec{u}) = m^{+} + m^{-}$$
 (6)

where m^+ and m^- denote the mass transfer rates of the vaporization and condensation (kg/m³/s), respectively.

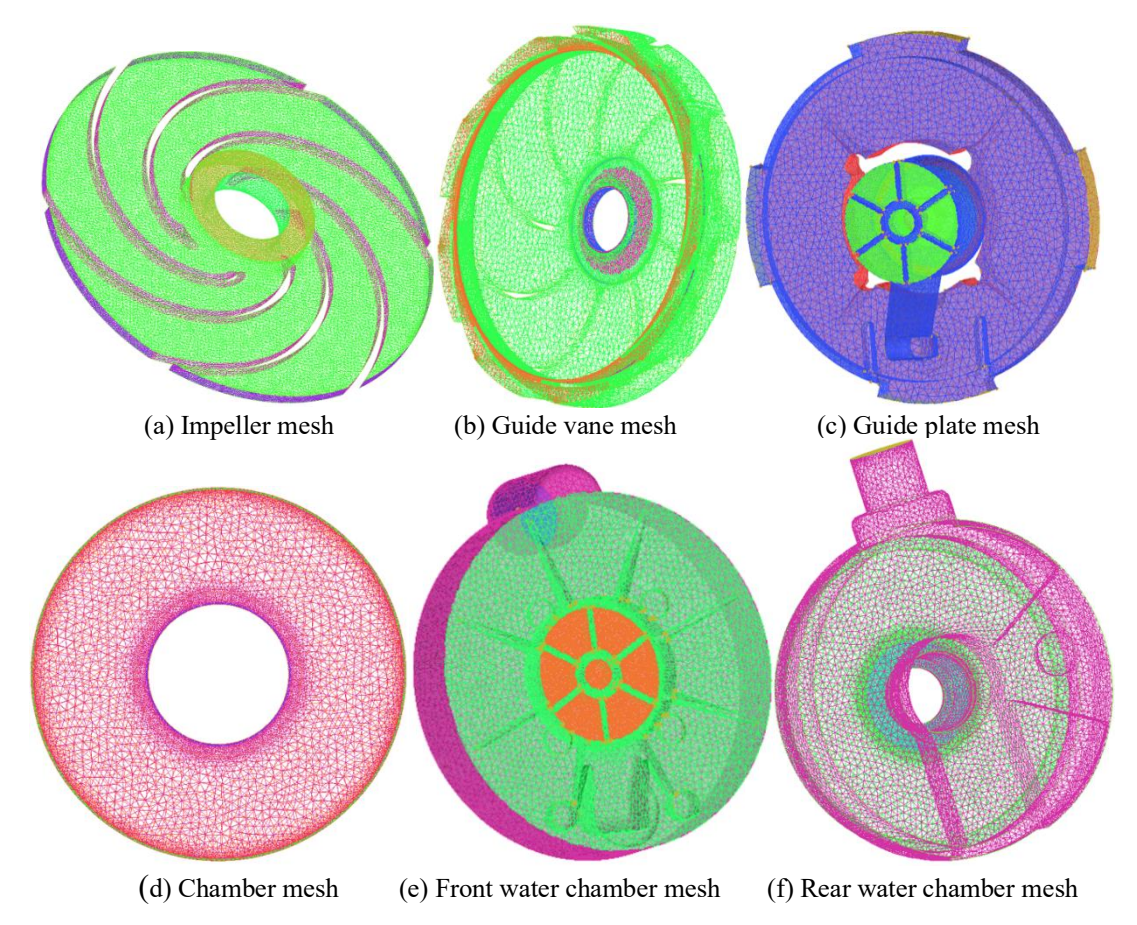


Fig. 2 Water mesh

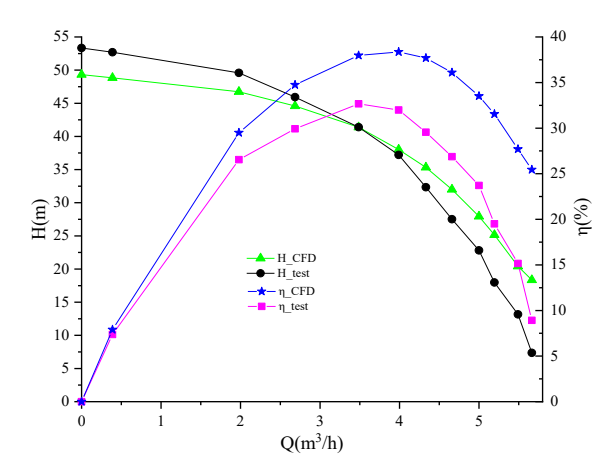


Fig. 3 Comparison between simulation and experiment

3. VERIFICATION AND ANALYSIS TO NUMERICAL CALCULATION RESULT

3.1 Numerical Calculation Verification

full-flow-field, multi-condition simulation of the five-stage centrifugal pump was conducted using CFX software. The computational domain was discretized into 40 units, including 5 impeller units and 5 auxiliary blade units rotating at 2800 rev/min, while the remaining water body units were set as static. Corresponding performance experiments were carried out to validate the numerical model. Figure 3 presents a comparison of simulated and experimental results for pump flow rate, head, and efficiency. Near the optimal operating point, the head deviation between simulation and experiment is only 0.02%, confirming high simulation accuracy in this region. However, deviation increases in high- and low-flow regions: Low-flow Experimental head exceeds simulated head, with deviation worsening as flow rate moves further from the optimal point. High-flow region: Experimental head falls below simulated head, with deviation increasing with flow rate deviation. The efficiency data in Fig. 3 represent hydraulic efficiency only, excluding energy losses during motor-topump power transmission. While simulated experimental efficiency trends align, with similar optimal operating points, significant deviations persist due to the exclusion of mechanical losses in the simulation.

3.2 Study on Steady-state Cavitation Performance

3.2.1 Cavitation Calculation Model

This study employs the Homogeneous Equilibrium Cavitation Model for cavitation calculations. The internal flow in multi-stage centrifugal pumps is characterized as three-dimensional turbulent flow, modeled using the k- ε turbulence model. Several commonly used cavitation models are derived from the Rayleigh-Plesset equation, with the model formula presented as follows: (Zhou et al., 2022)

$$R_{e} = F_{vap} \frac{3a_{nuc}(1 - a_{v})\rho_{v}}{R_{B}} \sqrt{\frac{2}{3} \frac{p_{v} - p}{\rho 1}}, \quad p \le p_{v}$$
(7)

$$R_{c} = F_{cond} \frac{3a_{v}\rho_{v}}{R_{B}} \sqrt{\frac{2}{3} \frac{p_{v} - p}{\rho_{1}}}, \quad p > p_{v}$$
(8)

where, R_c is the steam generation rate; R_c is the steam condensation rate; F_{vap} is the empirical correction coefficient for vaporization process; F_{cond} is the empirical correction coefficient for the condensation process; R_B is the radius of the bubble, m; P_v is the vaporization pressure, Pa; a_{ruc} is the volume fraction of the nucleation site.

3.2.2 Numerical Simulation Settings

CFX was employed for both steady-state and transient cavitation numerical simulations of the multistage centrifugal pump, with total pressure inlet and velocity outlet boundary conditions specified. Cavitation was deemed to occur when the total inlet pressure gradually decreased, causing the pump head to drop by 3% relative to the non-cavitation calculation value. A no-slip wall condition was applied, with the water body in the impeller and the front chamber of the auxiliary blade impeller designated as rotating domains, while other water bodies were set as stationary domains. The dynamic-static interface between the stationary and rotating water bodies was modeled using the frozen rotor approach. The liquid medium was defined as water at 25 °C, and the gas medium as water vapor at 25 °C. At the inlet, the volume fraction of the liquid phase was set to 1, and that of the water vapor phase to 0. The saturated vapor pressure of water at 25 °C was defined as Pv=3169Pa, with a reference pressure of 0 Pa. Initially, steady-state cavitation calculations were performed, and the results were used as the initial field for subsequent transient cavitation simulations. The transient calculations typically reached a stable state after four rotational cycles; thus, six complete rotation cycles were computed in this study, with results from the sixth cycle extracted for cavitation mechanism analysis. Each 1° rotation of the impeller corresponded to a time step of 0.0000595238s. Each time step underwent 10 iterations, resulting in a total simulation time of 0.128571429s. The rotational period of the impeller, denoted as T (shaft period), corresponds to the shaft frequency; T1 represents the period for the impeller to rotate past a fixed position (blade period), corresponding to the blade frequency; and T2 denotes the pulsation period, calculated as $T2=T/9\times2$, corresponding to the pulsation frequency. The impeller rotation period T was 0.021428571(s), with 360 time steps per cycle. The pulsation period T2 was 0.00119(s). The shaft frequency f=1/T=46.7(Hz), the blade frequency f=1/T=280(Hz), and the pulsation frequency f2=1/T2=840(Hz). The convergence criterion was set to 10^{-4} .

Cavitation in multi-stage centrifugal pumps can induce severe pressure pulsations, leading to cavitation noise and resonance issues. To monitor transient pressure pulsations, monitoring points were established on the water body surface, as illustrated in Fig. 4. These points were located at the center of the pump inlet and outlet, on the surface of the first-stage impeller blade, and at the outlet of each impeller stage.

4. ANALYSIS OF CAVITATION STATE

4.1 Basic Theory of Cavitation

The occurrence of cavitation in centrifugal pumps depends on both the pump design and the suction device,

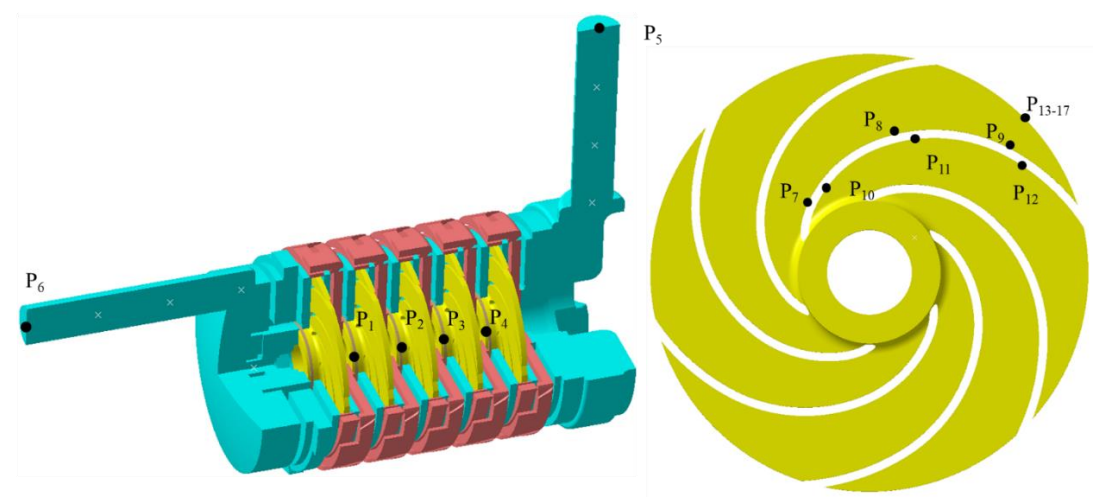


Fig. 4 Pressure monitoring points

and is governed by two key parameters: the NPSH available $(L_{\rm NPSHa})$ and the NPSH required $(L_{\rm NPSHr})$. The NPSH available $(L_{\rm NPSHa})$ represents the net positive suction head supplied by the suction system to the pump inlet, reflecting the excess energy of the liquid above its vaporization pressure. The NPSH required $(L_{\rm NPSHr})$ is the minimum net positive suction head required for the pump to operate normally at a given speed and flow rate, reflecting the pressure losses caused by the pump's internal structure. The cavitation conditions are as follows:

 $L_{\text{NPSHa}} > L_{\text{NPSHr}}$: No cavitation occurs.

 $L_{\text{NPSHa}} = L_{\text{NPSHr}}$: Cavitation begins.

 $L_{\text{NPSHa}} < L_{\text{NPSHr}}$: Severe cavitation occurs.

From this relationship, it is evident that $L_{\rm NPSHa} = L_{\rm NPSHr}$ marks the critical point for cavitation onset. Therefore, improving the cavitation performance of centrifugal pumps can be achieved by either increasing $L_{\rm NPSHa}$ or reducing $L_{\rm NPSHr}$. The relevant formulas are defined as follows:(Li F., et al. 2022)

$$L_{NPSHa} = \frac{p_s}{\rho g} + \frac{V_s^2}{2g} - \frac{p_v}{\rho g} = \frac{p_c}{\rho g} \pm h_g - h_c - \frac{p_v}{\rho g}$$
 (9)

$$L_{NPSH_r} = \frac{p_s}{\rho g} + \frac{v_s^2}{2g} - \frac{p_k}{\rho g} = \frac{v_0^2}{2g} + \lambda \frac{w_0^2}{2g}$$
 (10)

where, P_s is the absolute pressure of the water flow at the pump inlet, (P_a) ; V_s is the average velocity of the water flow at the pump inlet, (m/s); P_v is the vaporization pressure of the medium corresponding to the temperature of the conveying medium, (P_a) ; P_c is the absolute pressure of the suction liquid surface, (P_a) ; h_g is the installation height of the pump, taking "-" for suction and "+" for backflow, (m); h_c is the hydraulic loss of the inlet pipeline, (m); P_k is the absolute pressure at the lowest pressure point inside the pump, (P_a) ; V_0 is the average absolute velocity of the liquid flow before entering the blades, (m/s); W_0 is the average relative velocity of the liquid flow before entering the blade, (m/s); λ is the pressure drop coefficient at the inlet of the blade.

4.2 Analysis of Cavitation State under Different Flow Rates

When the pressure of water in the multi-stage

centrifugal pump falls below the saturated vapor pressure of 3169 Pa at 25°C, vaporization occurs, generating bubbles that mix with the surrounding water and fill the internal flow passages, resulting in a reduction in pump head. The the NPSH available ($L_{\rm NPSHa}$) and head under different flow rates are presented in Table 1. The comparison of effective cavitation allowance and head ($L_{\rm NPSHa}$ -H) curves at different flow rates, and the critical cavitation allowance and head at different flow rates are shown in Table 2.

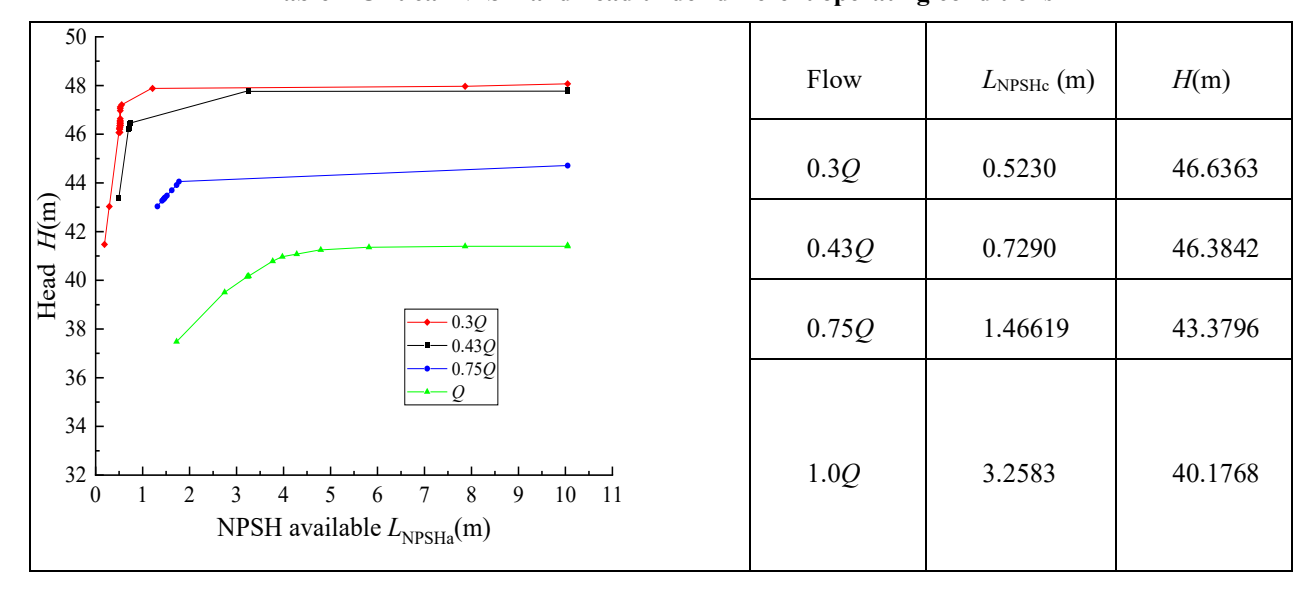
The data indicate that as inlet pressure decreases, the pump's the NPSH available (L_{NPSHa}) also decreases. When L_{NPSHa} remains relatively high, the pump head remains largely unchanged. However, as L_{NPSHa} gradually declines, the pump head experiences a sharp drop at a certain threshold. This occurs because when the water pressure at the impeller inlet drops below 3169 Pa, part of the water vaporizes. Initially, with minimal gas entrainment, the pump head remains stable, though cavitation noise may be present. As gas entrainment increases significantly, the volume of water passing through the impeller per unit time decreases, reducing the total energy transferred from the impeller's mechanical energy to the water. This is accompanied by internal backflow within the impeller flow field, ultimately leading to a head reduction. When the flow rate increases, the pump head decreases, while the corresponding critical NPSH increases, resulting in reduced anti-cavitation performance. Comparing different flow conditions, the operating point at 1.0Q exhibits the highest critical NPSH and corresponding head, whereas the operating point at 0.3Q shows the lowest. Specifically, when the flow rate decreases to 0.30, the critical NPSH (L_{NPSHc}) is only 16% of that under the Q condition. Therefore, under varying operating conditions, the auxiliary blade structure demonstrates better anticavitation performance and higher corresponding head at lower flow rates.

For the auxiliary blade structure pump operating at the design flow rate Q, the critical NPSH ($L_{\rm NPSHc}$) is 3.26 m, with a corresponding head of 40.18m upon cavitation onset. At a design flow rate of 0.3Q, the critical NPSH ($L_{\rm NPSHc}$) is 0.52m, with a corresponding head of 46.64m when cavitation occurs.

Flow 0.3 <i>Q</i>			Flow 0.43 <i>Q</i>		Flow 0.75 <i>Q</i>			Flow Q			
L _{NPSHa} (m)	$H(\mathbf{m})$	LR (%)	L _{NPSHa} (m)	$H(\mathbf{m})$	LR (%)	L _{NPSHa} (m)	H(m)	LR (%)	L _{NPSHa} (m)	H (m)	LR (%)
10.0479	48.07	0.00	10.0479	47.81	0.00	10.0479	44.71	0.00	10.0479	41.44	0.00
7.8649	47.97	0.21	10.0479	47.77	0.08	1.7741	44.06	1.47	7.8648	41.40	0.10
1.2111	47.88	0.39	3.2584	47.76	0.10	1.6205	43.70	2.27	5.8175	41.35	0.20
0.5549	47.21	1.79	0.7402	46.46	2.81	1.5181	43.48	2.76	4.7938	41.25	0.45
0.5230	46.64	2.98	0.7290	46.38	2.97	1.4662	43.38	2.98	3.2583	40.18	3.04
0.5229	46.46	3.36	0.7156	46.26	3.22	1.4454	43.33	3.11	3.2276	40.15	3.10
0.5228	46.43	3.41	0.6993	46.21	3.33	1.4157	43.27	3.23	2.7465	39.51	4.65
0.5225	46.37	3.54	0.4946	43.39	9.23	1.3136	43.04	3.75	1.7228	37.48	9.55

Table 1 NPSH available and head under different operating conditions $L_{\rm NPSHa}$ -H

Table 2 Critical NPSH and head under different operating conditions



4.3 Steady State Cavitation Characteristics under Low Flow Conditions

Multi-stage centrifugal pumps exhibit strong anticavitation performance under low flow conditions and are commonly employed in applications requiring low flow rates and high heads. This section investigates steady-state cavitation behavior at a low flow rate of $1.08 \mathrm{m}^3/\mathrm{h}~(0.3 Q)$ to reveal internal flow patterns under such conditions.

4.3.1 Comparative Analysis of Pressure

Table 3 presents pressure contours of the impeller section for an auxiliary-blade pump under three inlet total pressure conditions: 15000 Pa, 10000 Pa, and 6000 Pa. The analysis reveals the following observations: At 15,000 Pa inlet pressure: A small blue low-pressure zone appears on the suction surface near the blade inlet, where pressure falls below the saturated vapor pressure of water at 25°C (3169 Pa). Cavitation initiates near the suction surface and extends outward along the blade. A large red high-pressure zone is present in the positive guide vane flow channel around the impeller, indicating high head generation. At 10000 Pa inlet pressure: The blue low-pressure area expands to fill the entire impeller inlet flow

channel, signifying increased cavitation extent within the impeller. This cavitation reduces water pressure inside the impeller and the outer edge guide vanes, as some regions have transitioned to vapor, lowering overall water energy. At 8277.5 Pa inlet pressure: The pump head decreases by 3%, marking the cavitation inception point. At 6000 Pa inlet pressure (severe cavitation): The blue low-pressure zone dominates most of the impeller flow channel, indicating extensive cavitation. A localized low-pressure area forms at the outer edge of the impeller water body, creating unstable alternating high- and low-pressure regions. Water pressure at the outer edge drops significantly, and the red high-pressure zone disappears from the positive guide vane, reflecting a substantial head reduction. Under this condition, unstable pressure alternation occurs around the auxiliary-blade impeller water body, indicating degraded flow stability.

Table 4 presents a comparative analysis of the surface pressure contours for the first-stage impeller blades under varying inlet total pressures (15000 Pa, 10000 Pa, and 6000 Pa) in the auxiliary blade scheme. As the inlet total pressure decreases from 15,000 Pa to 6,000 Pa, the low-pressure zone near the blade inlet progressively

Unit Pa

6.40x10² 1.04x10⁴ 2.01x10⁴ 2.98x10⁴ 3.95x10⁴ 4.92x10⁴ 5.90x10⁴ 6.87x10⁴ 7.84x10⁴ 8.81x10⁴ 9.78x10⁴ 1.08x10⁵ 1.17x10⁵ 1.27x10⁵

Total pressure

15000 (Pa)

60000 (Pa)

Table 3 Pressure contour comparison of first stage impeller section under different inlet total pressure

Table 4 Pressure contour comparison of first stage blades surface under different inlet total pressure

Unit Pa	$6.48 \times 10^2 \ 1.27 \times 10^4 \ 2.47 \times 10^4 \ 3.68 \times 10^4 \ 4.88 \times 10^4 \ 6.08 \times 10^4 \ 7.29 \times 10^4 \ 8.49 \times 10^4 \ 9.69 \times 10^4 \ 1.09 \times 10^5 \ 1.21 \times 10^5$							
Total pressure	15000 (Pa)	6000 (Pa)						

expands. At 15000 Pa inlet pressure, a small blue low-pressure area is observed solely on the suction surface near the blade inlet, indicating localized cavitation. The pressure surface maintains relatively high pressure, aligning with the cross-sectional pressure analysis of the impeller water body. When the inlet total pressure drops to 10000 Pa, the blue low-pressure zone on the suction surface enlarges significantly, and a distinct low-pressure area begins to form on the pressure surface near the inlet,

suggesting an expansion of the cavitation region within the impeller. At 6000 Pa inlet pressure, severe cavitation occurs, with most of the suction surface and half of the pressure surface covered by the blue low-pressure zone. The surface pressure at the outer edge of the impeller blades decreases markedly, reflecting a substantial deterioration in flow conditions. Overall, the surface pressure of the first-stage impeller blades undergoes significant changes as the inlet total pressure is reduced.

Unit Pa 8.90x10³ 2.09x10⁴ 3.29x10⁴ 4.49x10⁴ 5.69x10⁴ 6.90x10⁴ 8.10x10⁴ 9.30x10⁴ 1.05x10⁵ 1.17x10⁵ 1.29x10⁵

Total pressure 15000 (Pa) 6000 (Pa)

Table 5 Pressure contour comparison of the first stage in the front chamber with different inlet total pressure

Table 5 illustrates a comparative analysis of crosssectional water pressure in the front chamber of the firststage impeller under varying inlet total pressures (15000 Pa, 10000 Pa, and 6000 Pa) for the auxiliary blade scheme. As the inlet total pressure decreases from 15,000 Pa to 6000 Pa, a corresponding reduction in water pressure is observed within the front chamber. At an inlet total pressure of 15000 Pa, a prominent red high-pressure area is present in the positive guide vane channel outside the impeller, with water pressure decreasing gradually from the periphery toward the center. When the inlet total pressure drops to 10000 Pa, the water pressure decreases due to the combined effects of cavitation and reduced inlet pressure. The red high-pressure zone at the outermost edge diminishes significantly, indicating cavitation within the first-stage impeller, though the water pressure in the front chamber remains above the saturated vapor pressure of 3169 Pa, preventing cavitation in this region. At an inlet total pressure of 6000 Pa, the water pressure in the entire front chamber decreases notably, yet the minimum pressure remains above 3169 Pa, ensuring no cavitation occurs. A high-pressure zone forms on the pressure surface of the auxiliary blade, serving as the source of mouth ring leakage, with reduced reflux velocity nearby. Under the influence of the auxiliary blade, water in the front chamber experiences centrifugal force, flowing outward and lowering the pressure in the front chamber. A circular, symmetrically distributed low-pressure zone forms near the center of the impeller.

4.3.2 Comparative Analysis of Cavitation Contour

Table 6 displays the cavitation cloud diagram comparison for the first-stage impeller under varying inlet total pressures (15000 Pa, 10000 Pa, and 6000 Pa) with auxiliary blade schemes. As the inlet total pressure decreases from 15000 Pa to 6000 Pa, the cavitation area near the blade inlet progressively expands. At 15000 Pa inlet pressure, cavitation occurs only at the inlet section of the blade suction surface, covering a relatively small area. This localized cavitation extends outward along the

suction surface. In the positive guide vane flow channel at the impeller's outer edge, a blue low-cavitation zone is observed due to pressure remaining above the saturated vapor pressure of water at 25°C. When the inlet pressure drops to 10000 Pa, the cavitation zone begins to obstruct the impeller inlet area and expands significantly within the impeller. At 6000 Pa inlet pressure, severe cavitation develops across most impeller flow channels, leading to a sharp decline in pump performance and substantial cavitation losses. The flow within the impeller channels exhibits a pronounced gas-liquid mixed phase. The cavitation boundary comparison diagram for the firststage impeller visually illustrates these changes under the three operating conditions, highlighting the gradual expansion of the cavitation area as inlet pressure decreases. At 15000 Pa, cavitation remains confined to the suction surface inlet, representing the initial stage. At 10000 Pa, numerous air bubbles appear in the impeller inlet area, creating an unstable gas-liquid mixture flow outside the boundary, though the outer edge remains predominantly liquid. At 6000 Pa, severe cavitation dominates most impeller passages. Surface cavitation on the first-stage impeller blades also expands near the inlet as inlet pressure decreases. At 15000 Pa, only localized cavitation occurs on the suction surface inlet area. At 10000 Pa, the cavitation area grows significantly, with some pressure surfaces also showing cavitation. At 6000 Pa, most suction and pressure surfaces turn red, indicating severe cavitation within the impeller water.

Table 7 compares cavitation in the front chamber water section of the first-stage impeller under varying inlet total pressures. As inlet pressure decreases from 15,000 Pa to 6,000 Pa, no cavitation occurs in the front chamber water body. This is because the front chamber water connects to the positive guide vane water, where high internal pressure transmits to the front chamber, maintaining elevated water pressure. Even when the auxiliary blade expels water from the front chamber, the resulting pressure drop remains insufficient to cause water vaporization.

Table 6 Cavitation comparison in the first stage impeller section of under different inlet total pressure

	 -	stage impener section of under							
	$9.90x10^{-16} \ 6.17x10^{-2} \ 1.23x10^{-1} \ 1.85x10^{-1} \ 2.47x10^{-1} \ 3.08x10^{-1} \ 3.70x10^{-1} \ 4.32x10^{-1} \ 4.94x10^{-1} \ 5.55x10^{-1} \ 6.17x10^{-1}$								
Total									
pressure	15000 (Pa)	10000 (Pa)	6000 (Pa)						
Cavitation of the first stage impeller section									
First stage impeller cavitation boundary									
Surface cavitation of the first stage impeller blades									

Table 7 Cavitation comparison of the first sage impeller front chamber section with different inlet total pressure

	9.90x10 ⁻¹⁶ 4.11x10 ⁻⁵ 8.22x10 ⁻⁵ 1.23x10 ⁻⁴ 1.64x10 ⁻⁴ 2.05x10 ⁻⁴ 2.47x10 ⁻⁴ 2.88x10 ⁻⁴ 3.29x10 ⁻⁴ 3.70x10 ⁻⁴ 4.11x10 ⁻⁴									
Total pressure	15000 (Pa)	10000(Pa)	6000 (Pa)							

4.3.3 Comparative Analysis of Velocity Vectors

Table 8 presents a comparison of velocity vectors in the first-stage impeller sections under varying inlet total pressures. The figure illustrates the velocity vector diagram of the internal flow field with auxiliary blade configurations at different inlet pressures. As the total inlet pressure decreases from 15000 Pa to 6000 Pa, the flow velocity within the blade channels gradually diminishes, and unstable turbulence emerges. The region with notable velocity vector changes is highlighted with a blue box in the figure. When the total inlet pressure is 15000 Pa, the velocity vectors throughout the flow channel remain relatively stable, characterized by high inlet velocity and low outlet velocity, forming a localized high-speed zone at the inlet of the positive guide vane. When the inlet pressure drops to 10000 Pa, the high-speed area within the flow channel begins to shrink. Unstable turbulence appears near the impeller outlet, altering the fluid flow direction and consuming energy input by the pump. When the total inlet pressure is 6000 Pa, the flow velocity inside the impeller decreases significantly, and extensive turbulence is generated at the outlet, leading to high energy consumption.

Table 9 shows the velocity vector diagram of the water section in the front chamber of the first-stage impeller under different inlet total pressures. It can be observed that as the total inlet pressure decreases from 15000 Pa to 6000 Pa, the flow velocity of water entering the front chamber from the positive guide vane decreases. This is attributed to the progressively severe cavitation within the impeller, which reduces the head generated by the first-stage impeller and decreases the leakage capacity of the mouth ring, resulting in slower water entry into the impeller front chamber. When the total inlet pressure is

15000 Pa and 10000 Pa, the small cavitation area has minimal impact on the leakage of water in the front chamber. However, when the total inlet pressure is 6000 Pa, the peripheral flow velocity of the entire front chamber water body decreases significantly, becoming notably lower than that observed at the two higher inlet pressures. At the position indicated by the arrow, which corresponds to the outer area of the blade suction surface, the color indicates a significant decrease in velocity. The pressure surface of the auxiliary blade can alter the water flow direction and increase the internal energy of the water. Consequently, the flow velocity of water around the front cavity with an auxiliary blade structure is significantly higher than that without an auxiliary blade structure.

4.3.4 Comparative Analysis of Turbulent Kinetic Energy

Table 10 presents the specific turbulent energy contours for the first-stage impeller section under different inlet total pressures. As observed from the figure, when the total inlet pressure decreases from 15000 Pa to 6000 Pa, the turbulent energy dissipation within the impeller channel gradually intensifies. At an inlet pressure of 15000 Pa, cavitation initiates inside the impeller, leading to significant turbulent energy losses near the impeller inlet area. However, the highest dissipation of turbulent energy occurs in the dynamic-static coupling region between the moving water body of the impeller and the static water body of the guide vane. When the total inlet pressure drops to 10000 Pa, the high turbulence energy dissipation zone has already filled the flow channel at the impeller inlet, indicating an expansion of the cavitation area within the impeller. At an inlet pressure of 6000 Pa, almost the entire impeller flow channel is filled with areas of high turbulence energy loss, signifying severe

Unit m/s

Total pressure

Total area

Zoomed view

Table 8 Vectors comparison of first stage impellers section with different inlet total pressure

Unit m/s

Total pressure

15000 (Pa)

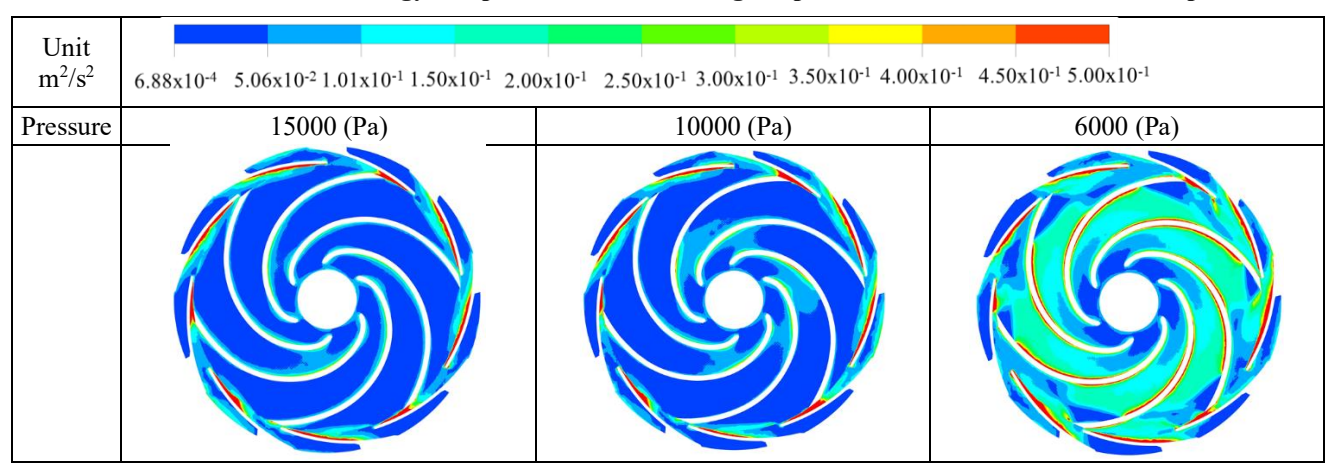
10000 (Pa)

6000 (Pa)

6000 (Pa)

Table 9 Vectors comparison of the first stage impeller front chamber section with different inlet total pressure

Table 10 Turbulent kinetic energy comparison of the first stage impeller section under different inlet pressures



cavitation within the impeller water. At this point, the turbulence energy dissipation throughout the impeller water is high, with an alternating pattern of high and low turbulence energy dissipation at the outer edge of the impeller, indicating an unstable flow field in this region. Consistent with the velocity vector analysis, the dynamic-static coupling area at the outermost edge of the impeller water exhibits the highest turbulence energy dissipation.

Table 11 compares the turbulent energy in the water section of the front chamber of the first-stage impeller under different inlet total pressures. As the total inlet pressure decreases from 15000 Pa to 6000 Pa, the turbulent energy dissipation within the water body in the impeller front chamber gradually increases. At an inlet pressure of 15000 Pa, the highest dissipation of turbulent energy occurs in the dynamic-static coupling region between the moving water body of the impeller and the static water body of the guide vane. When the total inlet pressure of the pump decreases to 10000 Pa, the turbulent energy loss in the middle of the front chamber increases, albeit not significantly, while the turbulent energy consumption of the fluid near the mouth ring decreases. At an inlet pressure of 6000 Pa, the turbulent energy at the outer edge of the water in the front chamber of the impeller increases significantly, with a large red area appearing.

Near the mouth ring, a blue area with lower turbulent energy emerges, indicating that the turbulent energy of the internal water in the front chamber experiences increases and decreases during changes in the total inlet pressure, specifically an increase at the outer edge and a decrease near the mouth ring.

4.4 Transient Characteristics under Low Flow Conditions

4.4.1 Comparative Analysis of Cavitation Contour

Based on previous analysis, the auxiliary-blade pump demonstrates superior anti-cavitation performance during low-flow operation. This section delves into the transient evolution of the cavitation flow field in the auxiliary-blade scheme under low-flow conditions (Q = 0.72 m/s) and derives corresponding change patterns.

Table 12 displays the velocity vector diagram of the first-stage impeller water section in the auxiliary-blade pump at different rotation angles. The figure reveals severe eddies within the impeller water, with similar eddy severity observed at various rotation angles. Near the impeller working surface, streamlines are relatively smooth, predominantly laminar flow, indicating a relatively stable flow field. The vortex area is primarily concentrated on the suction surface of the blades. Figure 5

Table 11 Turbulent kinetic energy of the front chamber in first stage impeller with different inlet pressures

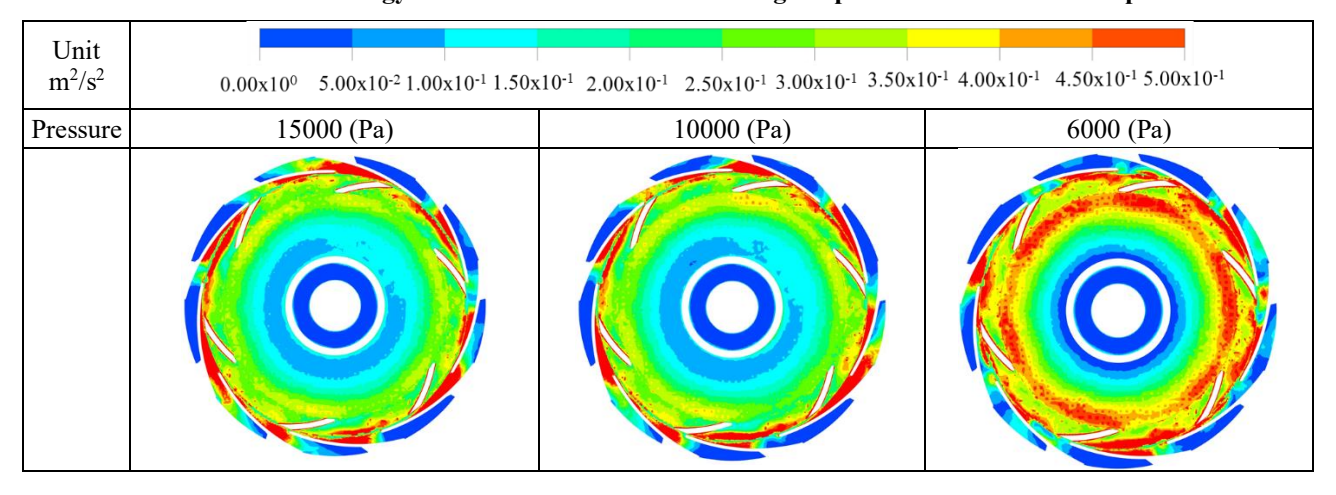
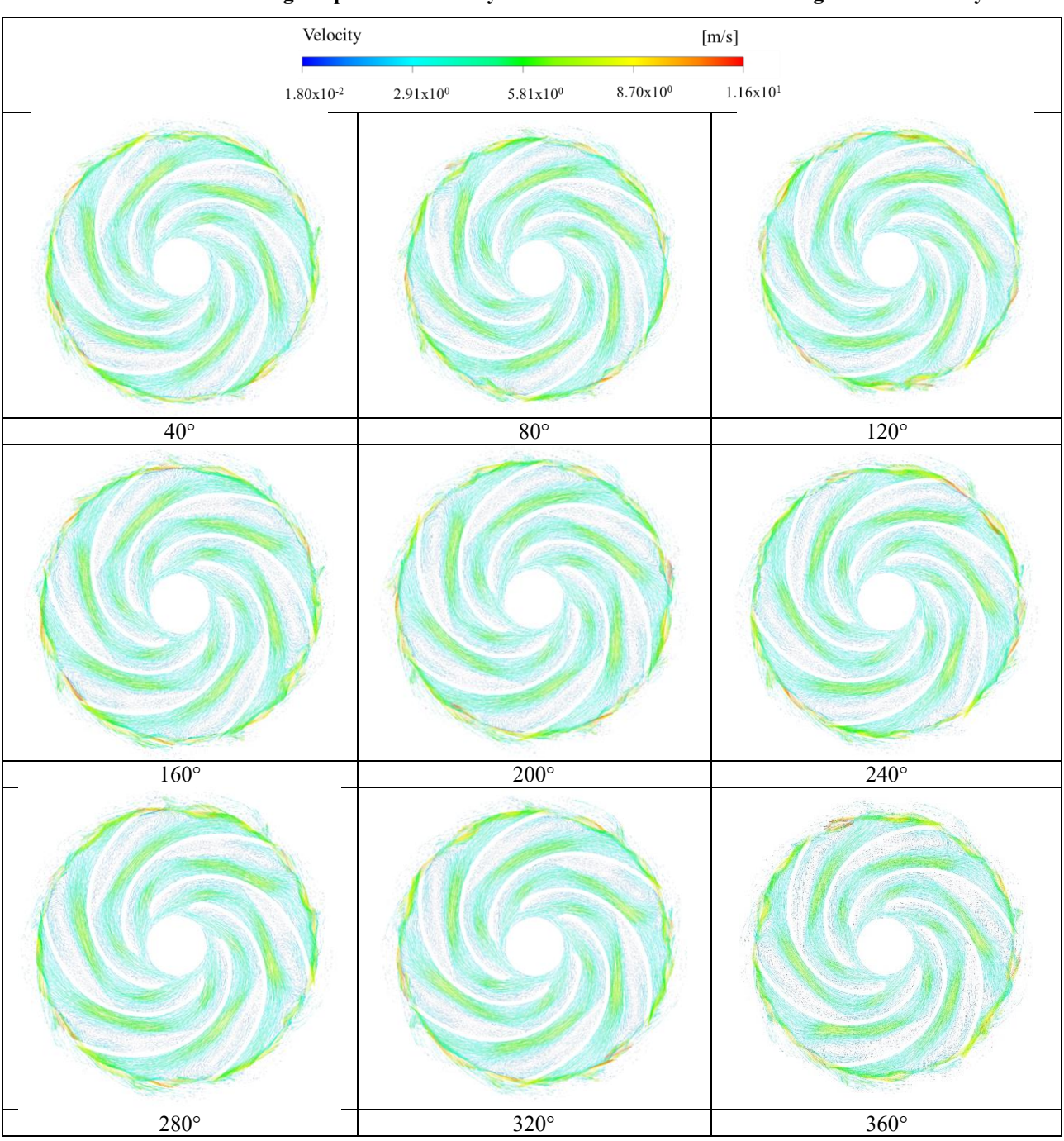


Table 12 Vector of the first stage impeller water body section with different rotation angles with auxiliary blades



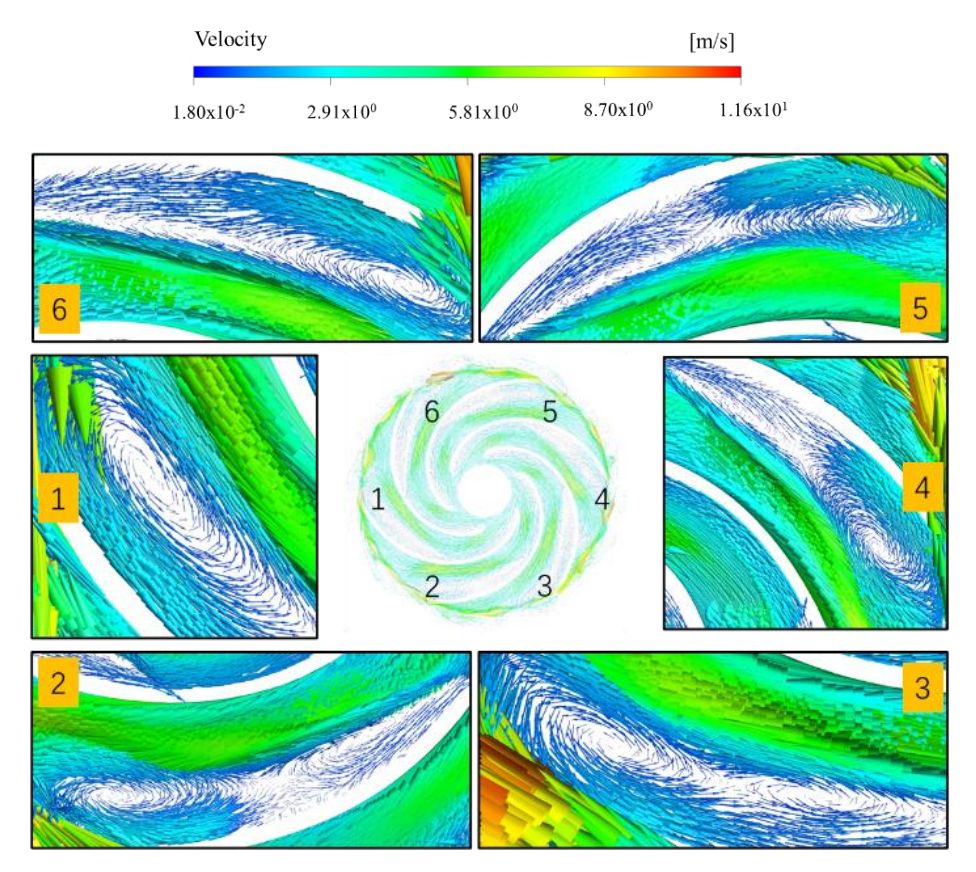


Fig. 5 Distribution of eddy in impeller water at 360 ° under cavitation conditions

provides an enlarged local view of the water vortex velocity vector inside the impeller at a 360° rotation. The figure shows varying degrees of vortices on the suction surface of each impeller, leading to significant energy loss. At positions marked 1 and 6, distinct large vortex structures form, while at positions marked 2 and 3, two vortex structures emerge on the suction surface of the blade, indicating non-uniform vortex structures across each channel.

Table 13 presents the pressure contour of the first-stage impeller water section in the auxiliary-blade pump at different rotation angles. Images are recorded every 40° rotation of the impeller, illustrating pressure changes during one full revolution. Throughout impeller rotation, the inlet remains consistently in the low-pressure to middle area, where severe cavitation occurs. Among these low-pressure zones, the blue zones at 40°, 160°, and 280° exhibit similar shapes, as do those at 80°, 200°, and 320°, and at 120°, 240°, and 360°. This indicates that these three groups have similar cavitation zones, forming a periodic cycle every 120° of impeller rotation. Pressure gradually increases from the impeller center outward, but the rate of pressure increase varies at each angle. At the starting position of 40°, the red high-pressure area inside the outer guide vanes of the impeller is the smallest. As the impeller rotates, this red high-pressure area inside the outer guide vanes begins to expand, then decreases again at 160°. The area of the red high-pressure zone changes over time at different angles, with the largest highpressure zone forming inside the positive guide vane at 280°. This suggests that after cavitation occurs in the

pump, the internal flow field still experiences a certain frequency of pulsation under fluid action.

Table 14 shows the cavitation contour of the firststage impeller water section in the auxiliary-blade pump at different rotation angles. During impeller rotation, the suction surface of the blade inlet is consistently in a severe cavitation state, with the cavitation area gradually extending from the suction surface to the pressure surface of the blade. In these cavitation regions, the shapes at 40°, 160°, and 280° are similar, as are those at 80°, 200°, and 320°, and at 120°, 240°, and 360°. This indicates that these three groups have similar cavitation regions, forming a periodic cycle every 120° of impeller rotation. The impeller gradually weakens from the center outward, with the outer edge being a blue non-cavitation area. When operating a multi-stage centrifugal pump under low-flow conditions, the suction surface of the blade inlet is the most prone to severe cavitation.

4.4.2 Pressure pulsation under low flow Cavitation state

Based on the preceding analysis, it can be concluded that cavitation occurring within the auxiliary blade pump induces significant vortex turbulence in the impeller's internal flow field, rendering it unstable. This section focuses on analyzing the pressure pulsation at the outlet of a multi-stage centrifugal pump, utilizing the auxiliary blade pump scheme. The pressure pulsation coefficient, denoted as $C_{\rm p}$, is defined as follows:

$$C_p = \Delta p / \left(0.5 \rho u_2^2\right) \tag{11}$$

Table 13 Pressure contour of the first stage impeller water body section with different angles

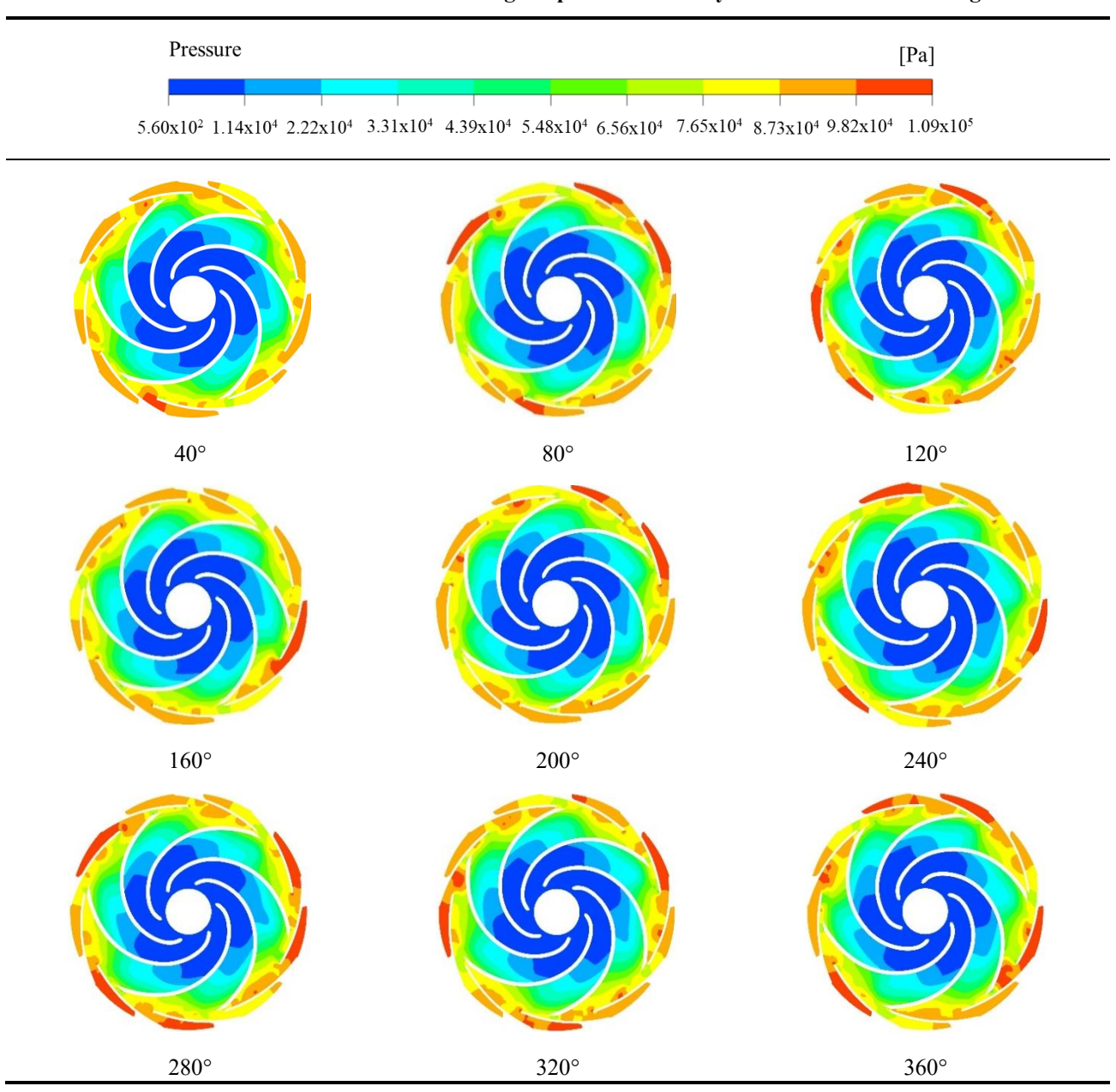
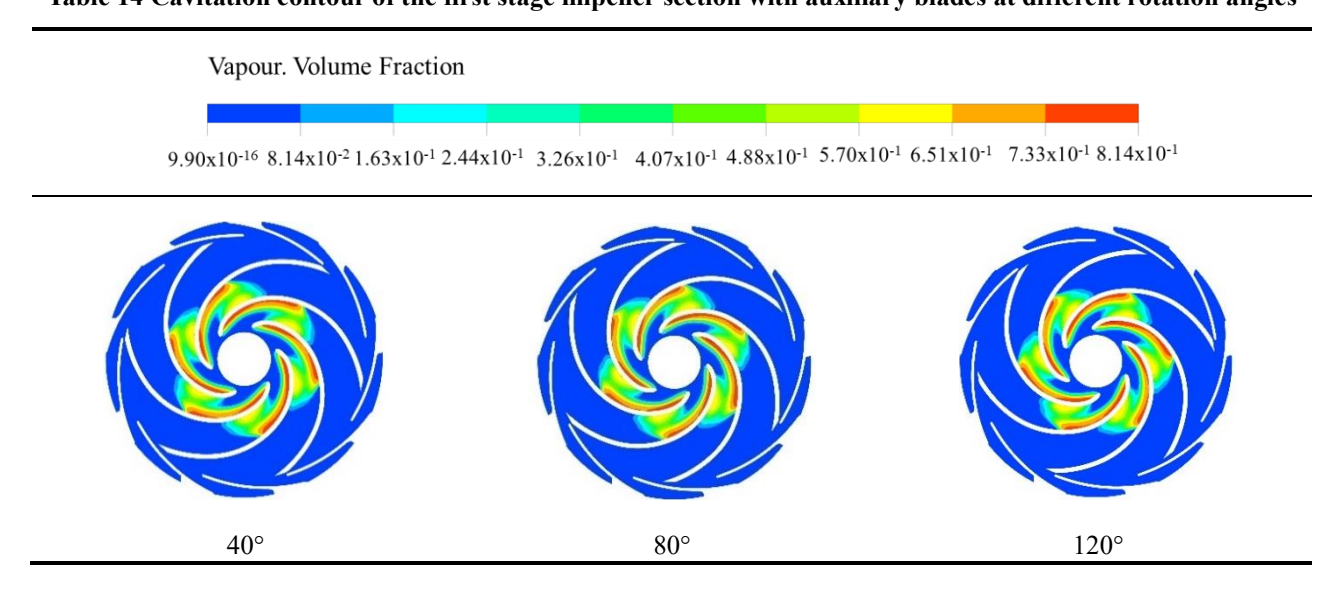
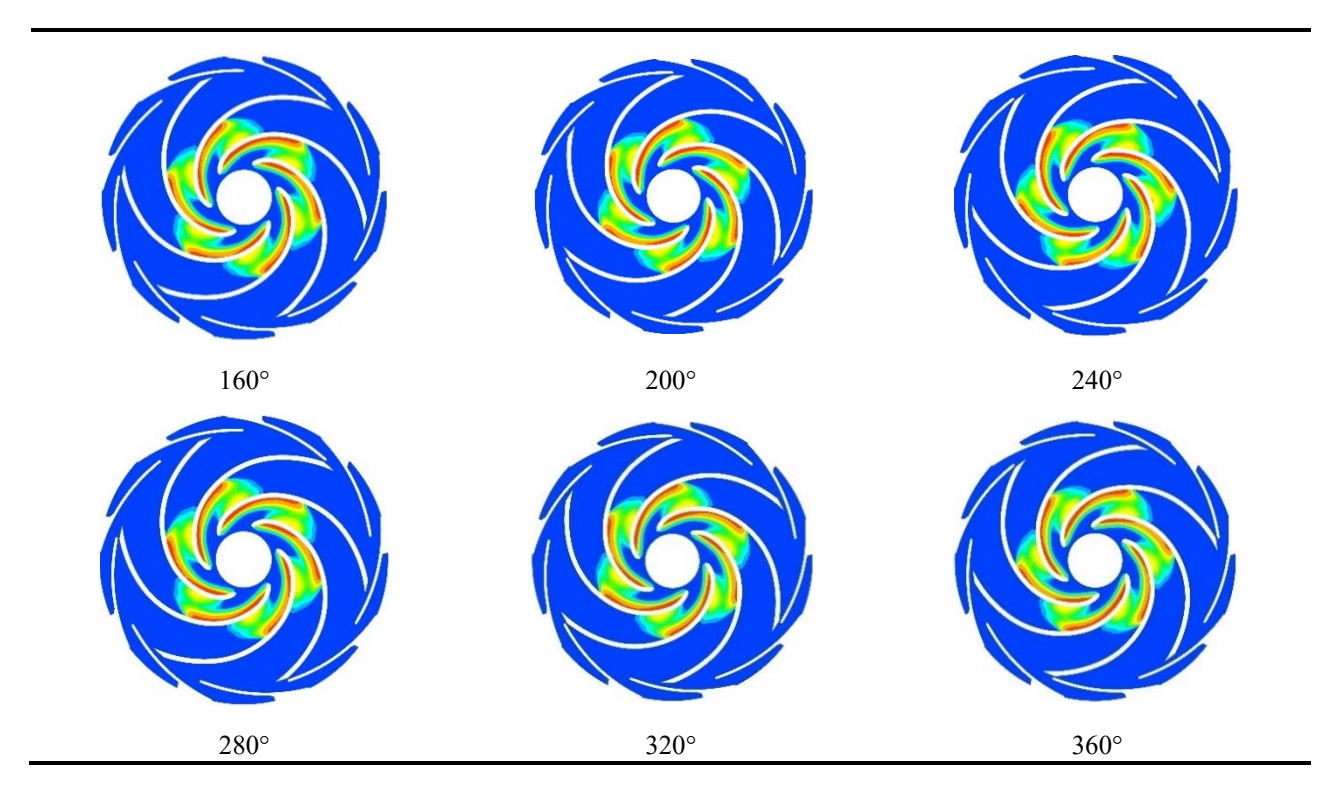


Table 14 Cavitation contour of the first stage impeller section with auxiliary blades at different rotation angles





Where, ΔP is the difference between the pressure at the monitoring point and its average value, Pa; ρ is the density, (kg/m³); u_2 is the circumferential velocity at the outlet of the impeller, (m/s).

Table 15 illustrates the time-domain graph of the outlet pressure for each stage guide vane under cavitation conditions. Monitoring points P1-P5 are situated at the

Monitor point pressure (Pa) 600000 600000 P1 P2 P3 P4 P5 30 74442 171974 264192 354984 452529 500000 500000 60 75345 173628 266607 355161 453317 173793 265584 350863 453707 400000 400000 Pressure (Pa) 172575 262721 345170 450904 300000 300000 150 79948 172013 261512 345122 449952 180 82725 171813 261620 348929 451166 200000 200000 210 76663 165282 256581 348120 450797 73230 164093 254976 347986 450363 100000 100000 76496 168009 259922 352644 454774 171302 262946 351311 452025 0 120 180 240 300 60 330 78756 171795 263567 352785 452770 Time step 360 79526 171479 261958 351004 448698

Table 15 Time diagram of outlet pressure of each stage pump under cavitation state

outlet of each pump stage, from the first to the fifth. Specifically, the monitoring points for the first to fourth stages are positioned at the guide vane outlet, while the monitoring point for the fifth stage is located at the center of the extended section of the pump outlet. As the impeller rotates, the pressure at the outlet of each guide vane stage fluctuates within a certain range. Due to severe cavitation within the impeller water, the flow becomes unstable, leading to superimposed pressure waveforms at the guide

vane outlet. Consequently, the pressure fluctuations at the guide vane outlet lack obvious periodicity. As the number of stages increases, the fluctuation range of the guide vane outlet pressure gradually widens, reaching its maximum at the pump outlet. This is attributed to the formation of a substantial gas-liquid mixture fluid in the first-stage impeller, generating an unstable pressure wave that propagates and intensifies through subsequent stages, resulting in higher pressure and a wider fluctuation range

at the outlet of each subsequent impeller. After cavitation occurs, the pressure increment at each stage remains relatively consistent.

Table 16 displays the time-domain graph of the pressure pulsation coefficient at the outlet of each stage guide vane under cavitation conditions. As depicted in the figure, during impeller rotation, the pressure pulsation

coefficient at the outlet of each guide vane stage fluctuates within a certain range. Due to severe cavitation within the impeller water, the pressure pulsation coefficient generated at the outlet of each guide vane stage is unstable and lacks obvious periodic characteristics. As the number of stages increases, the amplitude of the pressure pulsation coefficient at the guide vane outlet gradually rises, reaching its peak at the pump outlet.

Table 16 Time diagram of outlet pressure fluctuation coefficient under cavitation state

0.16	Step	Monitor point C_p				
0.16 F 0.14 F	ep	P1	P2	P3	P4	P5
0.12 $$ P_1 $$ P_2 $$ P_3 $$ P_5	30	-0.0267	0.0118	0.0214	0.0399	0.0038
0.10 0.08 A A A A A	60	-0.0188	0.0264	0.0427	0.0414	0.0107
0.06 [90	0.0007	0.0278	0.0337	0.0036	0.0141
0.04	120	0.0059	0.0171	0.0085	-0.0465	-0.0105
5° 0.02 F	150	0.0217	0.0122	-0.0021	-0.0469	-0.0189
-0.02	180	0.0461	0.0104	-0.0012	-0.0134	-0.0082
-0.04	210	-0.0072	-0.0471	-0.0455	-0.0205	-0.0115
-0.06 H V V V V V V V V V V V V V V V V V V	240	-0.0374	-0.0575	-0.0596	-0.0217	-0.0153
-0.10 [-	270	-0.0087	-0.0231	-0.0161	0.0193	0.0235
-0.12	300	0.0004	0.0059	0.0105	0.0076	-0.0007
0 60 120 180 240 300 360	330	0.0112	0.0102	0.0159	0.0205	0.0059
Time step	360	0.0112	0.0102	0.0018	0.0203	-0.0299
	300	0.0180	0.0073	0.0018	0.0049	-0.0299

Table 17 Frequency diagram of outlet pressure pulsation coefficient under cavitation state

	F	Monitor point amplitude				
0.070		\mathbf{P}_1	\mathbf{P}_2	\mathbf{P}_3	P_4	P_5
0.056	140	8.1E-03	1.1E-02	1.3E-02	1.2E-02	4.9E-03
0.042	g 280	2.7E-03	4.7E-03	6.4E-03	9.0E-03	1.1E-02
0.028	420	1.9E-03	3.6E-03	3.9E-03	4.2E-03	4.9E-03
0.014	560	4.4E-04	2.4E-03	4.9E-03	7.7E-03	8.9E-03
0,000	700	1.6E-03	1.6E-03	1.6E-03	1.9E-03	1.9E-03
PI	840	1.7E-02	3.3E-02	4.7E-02	5.9E-02	7.0E-02
P2 difference of the control of the	1680	1.9E-04	1.5E-03	2.7E-03	3.9E-03	5.5E-03
P3 P3 P4 state delta	2520	4.0E-05	2.4E-04	4.2E-04	4.6E-04	7.5E-04
PS	3360	6.1E-05	9.1E-05	1.9E-04	2.6E-04	4.6E-04
0 840 1680 2520 3360 4200 5040	4200	1.1E-04	1.8E-04	2.4E-04	3.3E-04	4.3E-04
Frequency Hz	5880	1.0E-04	5.2E-05	2.2E-05	3.1E-05	1.6E-05
	6720	6.0E-05	6.3E-05	8.1E-05	1.6E-04	1.7E-04

Table 17 presents the frequency domain diagram of the pressure pulsation coefficient at the outlet of each stage guide vane under cavitation conditions. As shown in the figure, during impeller rotation, the main frequency remains constant at 840 Hz, with the maximum amplitude occurring at this frequency. Large amplitude peaks are observed at integer multiples of the main frequency, and as the pulsation frequency increases, the amplitude gradually diminishes. High amplitude frequency bands are evident in the low-frequency region of each guide vane stage outlet, with a prominent high amplitude frequency domain point at the outlet of the first four guide vane stages. This is because, in the gasification state, there are

more turbulent pressure waves in the low-frequency region of the impeller cavity water, which transmit to each stage impeller outlet, creating a high amplitude region in the low-frequency region and a large peak. The fifth point, located at the pump outlet, benefits from a water storage chamber between the pump outlet end and the fifth stage guide vane, which produces a damping effect and significantly reduces the vibration amplitude in the low-frequency region. The amplitude of the first four low-frequency regions ranges between 0.02-0.03 and exhibits an increasing trend, while at the pump outlet, the vibration amplitude decreases to approximately 0.01, representing a maximum reduction of 2/3. It can be concluded that to

mitigate the low-frequency vibration peak caused by cavitation in multi-stage centrifugal pumps, damping can be enhanced by incorporating an outlet water storage chamber to stabilize the pressure pulsation at the pump outlet.

5. SUMMARY

Based on the Homogeneous Equilibrium Cavitation Model, a comprehensive study was conducted on the cavitation performance of auxiliary - blade centrifugal pumps, and the cavitation flow mechanism under low - flow conditions was thoroughly explored. Additionally, the transient cavitation flow evolution mechanism under the influence of auxiliary blades was analyzed. The main conclusions are as follows:

- (1) Through numerical simulation, the hydraulic performance of auxiliary blade pumps can be accurately calculated. For multi stage centrifugal pumps with the same auxiliary blade structure, as the flow rate decreases, the corresponding head increases, the critical NPSH decreases, and the anti cavitation ability strengthens. When the flow rate drops to 0.3Q, the critical NPSH is only 16% of that under the Q condition.
- (2) When severe cavitation occurs inside the impeller of a multi stage centrifugal pump with an auxiliary blade structure, gas liquid mixing takes place within the impeller, leading to the formation of severe vortices in the water inside. Under different inlet total pressure conditions, the initial cavitation position of the pump is located in the suction surface area of the blade inlet. As the inlet total pressure gradually decreases, the cavitation area expands from the suction surface of the blade and eventually extends to the entire impeller flow channel, resulting in a significant drop in the pump head.
- (3) The water in the front chamber of the first stage impeller of the auxiliary blade pump has a relatively high internal flow field pressure, and cavitation does not occur. After cavitation takes place, the peripheral flow velocity of the entire front chamber water body decreases significantly, being much lower than that in the non cavitation state. When cavitation occurs inside the impeller, the water in the front chamber of the impeller still maintains good cavitation stability.
- (4) After cavitation in multi stage centrifugal pumps, the internal water pressure fluctuates unstably. As the number of stages increases, the pressure fluctuation range at the outlet of each stage guide vane widens, and the amplitude of frequency domain vibration increases. Due to the damping effect of the water storage chamber at the pump outlet, the amplitude of low frequency vibration generated at the outlet of the multi stage centrifugal pump in the cavitation state is reduced, with the maximum vibration amplitude decreasing by 2/3.

ACKNOWLEDGMENTS

The work was sponsored by the National Natural Science Foundation of China International Cooperation

Key Research Project (No. 52120105010), the National Natural Science Foundation of China (No. 52179085).

CONFLICT OF INTEREST

The authors declare that there are no conflicts of interest.

AUTHORS CONTRIBUTION

Gao Yi: Conceptualization, methodology, supervision, visualization, data curation, formal analysis, writing—original draft; Zhang DiXiao: Data curation, validation, writing—original draft; Li Hui: Supervision; Zhu Xingming and Ruan Bing Er: Review & editing.

REFERENCES

- Ji, L., Li W., Shi W., Fei T., RA E. (2020c). Diagnosis of internal energy characteristics of mixed-flow pump within stall region based on entropy production analysis model. *International Communications in Heat and Mass Transfer*, 117. https://doi.org/10.1016/j.icheatmasstransfer.2020.10 4784.
- Al-Obaidi, A. R., & Shaban, A. H. (2024). Experimental and numerical effect of cavitation detection on hydraulic performance of the centrifugal pump based on different geometrical configurations. *Journal of Engineering*Research. https://doi.org/10.1016/j.jer.2024.11.006
- Chen, B., Yang, C., Zhang, H., Wang, Y., & Xia, C. (2021). Cavitation characteristics of high-speed submersible axial-flow pump. *Journal of Drainage and Irrigation Machinery Engineering*. https://doi.org/10.3969/j.issn.1674-8530.19.0319
- Fu, X., Li, D., Wang, H., Qin D., & Wei, X. (2023). Cavitation mechanism and effect on pump power-trip transient process of a pumped-storage unit. *Journal of Energy*Storage, https://doi.org/10.1016/j.est.2023.107405.
- Gao, Y., Li, W., Qi, H., Ji, L., & Chen, Y. (2023a). Optimized Design of a Multistage Centrifugal Pump Based on Volumetric Loss Reduction by Auxiliary Blades. *Water*, *15*(13), 18. https://doi.org/10.3390/w15132350.
- Gao, Y., Li, W., Ji, L., Cao, W., & Chen Y. (2023b). Optimization Design of Centrifugal Pump Auxiliary Blades Based on Orthogonal Experiment and Grey Correlation Analysis. *Water*, 15(13):25. https://doi.org/10.3390/w15132465.
- Gohir, P. P., & Saini, R. P. (2015). Effect of temperature, suction head and flow velocity on cavitation in a Francis turbine of small hydro power plant. *Energy*, 93 (DEC.PT.1), 613-624. https://doi.org/10.1016/j.energy.2015.09.042.
- He, X., Liu, H., & Tan, M. (2017). The influence of impeller back blade shape on the performance of molten salt pumps. *Journal of Irrigation and*

- *Drainage Mechanical Engineering, 35* (4). 289-295. https://doi.org/10.3969/j.issn.1674-8530.15.0288.
- Ji, L., He, S., & Agarwal, L. R. (2023). Exploration of Blade Thickness in Suppressing Rotating Stall of Mixed Flow Pump. Arabian Journal for Science and Engineering, 48(6), 8227-8251. https://doi.org/10.1007/s13369-023-07901-x.
- Ji, L., Li, W., Shi, W., Chang H., & Yang Z. (2020a). Energy characteristics of mixed-flow pump under different tip clearances based on entropy production analysis. *Energy*, 199, 117447. https://doi.org/10.1016/j.energy.2020.117447.
- Ji, L. Wei, L., Weidong, & S., Fei, T. (2020b). Ramesh Agarwal. Diagnosis of internal energy characteristics of mixed-flow pump within stall region based on entropy production analysis model. *International Communications in Heat and Mass Transfer*, 117, 0-104784.
 - $\frac{https://doi.org/10.1016/j.icheatmasstransfer.2020.10}{4784.}$
- Li, D., Zhu, Y., Lin, S., Gong, R., Wang, H., & Luo, X. (2022). Cavitation effects on pressure fluctuation in pump-turbine hump region. *Journal of Energy Storage*, 47. https://doi.org/10.1016/j.est.2021.103936.
- Li, G., Ding, X., Wu, Y., Wang S., Li D., Yu W., Wang X., Zhu Y., & Guo Y. (2022). Liquid-vapor two-phase flow in centrifugal pump: Cavitation, mass transfer, and impeller structure optimization. *Vacuum*, *201*, 111102. https://doi.org/10.1016/j.vacuum.2022.111102.
- Li, R., (2012). Numerical calculation for effects of impeller Back pump out vanes on axial thmst in screw centrifugal pump. *Journal of Mechanical Engineering*, 48(12), 156-161. (in Chinese) https://doi.org/10.3901/JME.2012.12.156.
- Li, W., Li, E., Ji, L., Zhou, L., Shi, W., & Zhu, Y. (2020). Mechanism and propagation characteristics of rotating stall in a mixed-flow pump. *Renewable Energy*, 153. https://doi.org/10.1016/j.renene.2020.02.003.
- Liu, Z., Chen, T., & Lu, W. (2019). Experiment and analysis for effects of impeller back Vanes on axial thrust of centrifugal pump. *Drainage and Irrigation Machinery*, 37(12). 1013-1018 . https://doi.org/10.3969/j.issn.1674-8530.18.0002.
- Liu, Z., Zhang, Y., Dai, Q., Zheng, Y., Wu, D., & Wei, W. (2022). Pressure pulsation characteristics and improvement methods of axial extension pump. *Journal of Drainage and Irrigation Machinery Engineering*, 40(1), 8-14. https://doi.org/10.3969/j.issn.1674-8530.20.0302.
- Lu, Y., Tan, L., Han, Y., & Liu, M. (2022). Cavitation-vibration correlation of a mixed flow pump under steady state and fast start-up conditions by experiment. *Ocean Engineering*, 1, 251. https://doi.org/10.1016/j.oceaneng.2022.111158.

- Qian, C., Luo, X., Yang, C., & Wang, B. (2021). Multistage pump axial force control and hydraulic performance optimization based on response surface methodology. *Journal of the Brazilian Society of Mechanical Sciences and Engineering*, 43(3). https://doi.org/10.1007/s40430-021-02849-1.
- Shi, G., Wang, S., Xiao, Y., Liu, Z., Li, H., & Liu, X. (2021). Effect of cavitation on energy conversion characteristics of a multiphase pump. *Renewable Energy*, 177. https://doi.org/10.1016/j.renene.2021.05.119.
- Si, Q., Liao, M., Qiu, N., Liang, Y., Yuan, J., & Yuan, S. (2022). Research progress on cavitation induced noise of centrifugal pump. *Journal of Ship Mechanics*, (005), 026. https://doi.org/10.3969/j.issn.1007-7294.2022.05.014.
- Song, P., Wei, Z., Zhen, H., Liu, M., & Ren, J. (2022). Effects of pre-whirl and blade profile on the hydraulic and cavitation performance of a centrifugal pump. *International Journal of Multiphase Flow*, https://doi.org/10.1016/j.ijmultiphaseflow.2022.1042
- Soyama, H. (2021). Luminescence intensity of vortex cavitation in a Venturi tube changing with cavitation number. *Ultrasonics Sonochemistry*, 71, 105389. https://doi.org/10.1016/j.ultsonch.2020.105389.
- Wei, X., Feng, Y., & Liu, K. (2022). Experimental study on the cavitation flow and vibration characteristics of circular arc gear pumps based on EEMD. *Journal of Vibration and Shock*, (041-010). https://doi.org/10.13465/j.cnki.jvs.2022.10.012.
- Xu, S., Wang, J., Chen, W., Ji, B., Yan, H., Zhang, Z., & Long, X. (2022). Removal of field-collected Microcystis aeruginosa in pilot-scale by a jet pump cavitation reactor. *Ultrasonics Sonochemistry*, 83, 105924. https://doi.org/10.1016/j.ultsonch.2022.105924.
- Xu, Z., Kong, F., Zhang, H., & Qiu N. (2021). Research on Visualization of Inducer Cavitation of High-Speed Centrifugal Pump in Low Flow Conditions. https://doi.org/10.3390/jmse9111240.
- Yan, L., Gao, B., & Ni, D. Z. N. Z. W. (2022). Numerical analysis on the cavitation characteristics of a pump with an inducer in non-uniform inflow. *Ocean Engineering*, 256(15), 111407.1-111407. 14. https://doi.org/10.1016/j.oceaneng.2022.111407.
- Yun, L., Rongsheng, Z., & Dezhong, W. A. (2020). Cavitation Performance Prediction Method for Pumps PART1-Proposal and Feasibility. *Nuclear Engineering and Technology*. https://doi.org/10.1016/j.net.2020.04.007.
- Zhao, G., Cao, L., Wu, R. Liang, N., & Wu, D. (2021). Wavelet-based multiresolution analysis of cavitationinduced loading instabilities under phase effect in a waterjet pump. *Ocean Engineering*, 15, 240. https://doi.org/10.1016/j.oceaneng.2021.109918.
- Zhao, G., Liang, N., Zhang, Y., Gao, L., & Wu, D. (2021).

- Dynamic behaviors of blade cavitation in a water jet pump with inlet guide vanes: Effects of inflow non-uniformity and unsteadiness. *Applied Ocean Research*, 117, 102889-. https://doi.org/10.1016/j.apor.2021.102889.
- Zhao, W., Li, Q., & Kang, Y. (2021). Effect of Suppressing Cavitation of Rough Zone on Suction Surface of Centrifugal Pump Blade. *Journal of Agricultural Machinery*, 52(6), 9. https://doi.org/10.6041/j.issn.1000-1298.2021.06.017.
- Zhao, W., Qin, J., Tian, X., & Wen, T. (2022). Cavitation characteristics of biomimetic centrifugal pump based on the "nodule effect" of humpback whales. *Transactions of the Chinese Society of Agricultural Engineering* (012), 038. https://doi.org/10.11975/j.issn.1002-6819.2022.12.003.
- Zhou, J., Pan, Q., et al. (2022). Transient start-up performance of mixed-flow pump and visual experimental study on cavitation flow field. *Journal of Irrigation and Drainage Mechanical Engineering*, 40 (3), 8.